Path-Following Control for Coordinated Turn Aircraft Maneuvers

David Cabecinhas[*] and Carlos Silvestre[†] and Paulo Rosa[‡] and Rita Cunha[§]

Instituto Superior Técnico, Institute for Systems and Robotics, 1049-001 Lisbon, Portugal

This paper addresses the path-following problem of steering an autonomous airplane along a predefined 3-D path, while performing a coordinated turn maneuver. The presented solution relies on the definition of a path-dependent error space to express the dynamic model of the vehicle, and of an output tracking error that guarantees both path-following and coordinated turn compliance. For controller design purposes, the error dynamics are approximated by a polytopic Linear Parameter Varying (LPV) system representation with piecewise affine dependency on the parameters. The synthesis problem is stated as an H_2 minimization problem with pole placement contraints, and solved using Linear Matrix Inequalities (LMIs). The nonlinear controller is implemented within the scope of gain-scheduling control theory, using the D-methodology. The performance of the designed controller is assessed in simulation, using the full nonlinear model of a small scale airplane.

I. Introduction

In recent years, the advent of enabling technology in sensing, computation, and communications has empowered Unmanned Aerial Vehicles (UAVs) to become cost-effective, reliable, and safe alternatives to conventional piloted aircraft in a wide variety of applications. For example, in forest fire surveillance, a small unmanned autonomous aircraft equipped with a camera and other sensing devices can be used to automatically detect fires and alert the nearest fire department. Other types of missions, where UAVs already play a key role, include surveillance and reconnaissance operations. These assignments are typically conducted in hostile and unexplored territory, where the risk of losing the aircraft is high. With UAVs, these missions can be accomplished without endangering human lives. Autonomous vehicles have great potential to perform high precision and repetitive tasks, since a whole new range of sensing devices can provide them with information that is not perceptible by a pilot. With this added information, autonomous flight control systems can be designed to provide enhanced performance and efficiency.

Several different approaches to the problem of flight control for autonomous aircraft can be found in the literature. For example, in References 1 and 2, nonlinear control strategies are used to address the trajectory-tracking problem, whereas Shue et al.[3] present a mixed H_2/H_∞ gain scheduling technique for aircraft control. A robust control solution for coordinated turn maneuvers is proposed in Reference 4.

This paper addresses the problem of aircraft control for coordinated turn maneuvers, using a path-following approach. By lifting the strict temporal restrictions that are dictated by a time-parameterized reference, the path-following approach provides an alternative to trajectory-tracking that typically results in smoother convergence to the path and less demand on the control effort. The coordinated turn maneuver improves the aircraft's flying qualities and performance, by constraining the vehicle's orientation to be such that there is no component of aerodynamic force along the y-axis of a body-fixed coordinate frame.[5] In this paper, the path-following problem is addressed along the lines of the work reported in References 6–8. It relies on applying a nonlinear transformation to aircraft dynamic model to obtain a conveniently defined error model. The resulting error vector comprises velocity errors, orientation errors, and the distance to the

---

[*]PhD Student, Department of Electrical Engineering and Computer Science (DEEC), Av. Rovisco Pais 1; dcabecinhas@isr.ist.utl.pt.

[†]Assistant Professor, DEEC, Av. Rovisco Pais 1; cjs@isr.ist.utl.pt. Member AIAA.

[‡]PhD Student, DEEC, Av. Rovisco Pais 1; prosa@isr.ist.utl.pt.

[§]PhD Student, DEEC, Av. Rovisco Pais 1; rita@isr.ist.utl.pt.

path, defined as the distance between the vehicle's position and its orthogonal projection on the path. In addition, an output tracking error to be driven to zero at steady-state is defined, which explicitly includes the coordinate turn constraint.

Having an accurate mathematical model of the airplane is an essential prerequisite for control system design. In this paper, we present SimAirDyn - an airplane dynamic model implemented in MATLAB/Simulink, which is specially suited for controller design. The most significant effects, which determine the aircraft's dynamic behavior and whose modeling requires special attention, are specified by the dimensionless aerodynamic force and torque coefficients. Typically, these coefficients are experimentally obtained in a wind tunnel. However, there are software alternatives to these tests, based on geometric models of the aircraft, which provide reasonable approximations for the coefficients with significant cost reduction. The latter approach was adopted to build the referred simulation model.

Airplanes are complex nonlinear systems whose dynamic behavior changes significantly as a function of the dynamic pressure, and angles of attack and side-slip. Thus, it is insufficient, for purposes of control system design, to represent them by simple Linear Time Invariant (LTI) models. Linear Parameter Varying (LPV) models represent nowadays a compromise between the global accuracy of nonlinear models and the straightforward controller synthesis techniques available for LTI representations. Partitioning the flight envelope into smaller regions, according to the relevant flight regime, simpler polytopic LPV models can be obtained, which are still accurate enough to capture the essential behavior of the aircraft and simultaneously provide the working ground for the control design phase.

The methodology used for performance analysis and controller synthesis builds on results described in References 9–11, which cast these problems into a Linear Matrix Inequality (LMI) framework. LMIs are steadily becoming a standard tool for advanced control system design, since both LMI feasibility and LMI-constrained optimization problems constitute convex optimization problems, for which efficient numerical solvers are available. In this paper, we synthesize a continuous-time state feedback H_2 controller subject to pole placement constraints for each of the operating regions, and implement a nonlinear gain-scheduling controller based on the D-methodology.[12]

The paper is organized as follows. Section II presents the standard rigid-body dynamic model, which is used to describe the aircraft. We also describe the derivation of the aircraft nonlinear dynamic model and analyze the natural modes obtained for the linearized model. Section III introduces the path-dependent error space and presents a derivation of the error dynamics. In Section IV, we describe the methodology used to compute H_2 controllers for polytopic LPV systems. The controller implementation using gain-scheduling and the D-methodology is also discussed. Finally, in Section V, we present simulation results for the closed-loop nonlinear aircraft model, under the presence of wind disturbances.

II. Aircraft Dynamic Model

This section presents the dynamic model of the unmanned aircraft depicted in Figure 1. The vehicle is equipped with a propeller and a set of control surfaces comprising the elevator, ailerons, and rudder.

Figure 1. Model-scale aircraft.

American Institute of Aeronautics and Astronautics

The aircraft is modeled as a 6 degrees of freedom rigid-body, moving with respect to the inertial frame $\{I\}$, and whose equations of motion are expressed in the body frame $\{B\}$ attached to the vehicle's center of mass. Let $({}^{I}\mathbf{p}_B, {}^{I}_{B}R) \in SE(3) \triangleq \mathbb{R}^3 \times SO(3)$ denote the configuration of $\{B\}$ with respect to $\{I\}$ and $\boldsymbol{\lambda}_B = [\phi_B \ \theta_B \ \psi_B]^T$, $\theta_B \in \ ]-\pi/2, \pi/2[$, $\phi_B, \psi_B \in \mathbb{R}$ denote the Z-Y-X Euler angles, representing the orientation of $\{B\}$ relative to $\{I\}$. The rotation matrix ${}^{I}_{B}R$ and the Euler angles $\boldsymbol{\lambda}_B$ satisfy

$$
{}^{I}_{B}R = R_Z(\psi_B)R_Y(\theta_B)R_X(\phi_B) \Leftrightarrow \boldsymbol{\lambda}_B = \arg({}^{I}_{B}R) \Leftrightarrow
\begin{cases}
\theta_B = \mathrm{atan2}(-r_{31}, \sqrt{r_{11}^2 + r_{21}^2}) \\
\phi_B = \mathrm{atan2}(r_{32}, r_{33}) \\
\psi_B = \mathrm{atan2}(r_{21}, r_{11})
\end{cases},
\tag{1}
$$

where $\mathrm{atan2}(.,.)$ denotes the four quadrant arctangent function and $R_Z(.)$, $R_Y(.)$, and $R_X(.)$ denote rotation matrices about the Z, Y, and X axes, respectively.

Consider also the linear and angular body velocities, $\mathbf{v}_B = [u \ v \ w]^T$ and $\boldsymbol{\omega}_B = [p \ q \ r]^T \in \mathbb{R}^3$, given respectively by $\mathbf{v}_B = {}^{B}_{I}R \, {}^{I}\dot{\mathbf{p}}_B$ and $\boldsymbol{\omega}_B = {}^{B}_{I}R \, {}^{I}\boldsymbol{\omega}_B$, where ${}^{I}\boldsymbol{\omega}_B \in \mathbb{R}^3$ denotes the angular velocity of $\{B\}$ with respect to $\{I\}$ expressed in $\{I\}$. According to this notation, the standard equations for the vehicle's kinematics[13] can be written as

$$
\begin{cases}
{}^{I}\dot{\mathbf{p}}_B = {}^{I}_{B}R \, \mathbf{v}_B \\
\dot{\boldsymbol{\lambda}}_B = Q(\phi_B, \theta_B)\,\boldsymbol{\omega}_B
\end{cases},
\tag{2}
$$

where

$$
Q(\phi_B, \theta_B) =
\begin{bmatrix}
1 & \sin\phi_B \tan\theta_B & \cos\phi_B \tan\theta_B \\
0 & \cos\phi_B & -\sin\phi_B \\
0 & \sin\phi_B/\cos\theta_B & \cos\phi_B/\cos\theta_B
\end{bmatrix},
\tag{3}
$$

and the derivative of ${}^{I}_{B}R$ is given by ${}^{I}_{B}\dot{R} = {}^{I}_{B}R \, S(\boldsymbol{\omega}_B)$, where $S(x) \in \mathbb{R}^{3\times3}$ is a skew symmetric matrix such that $S(x)\,y = x \times y$, for all $x, y \in \mathbb{R}^3$. Using the Newton-Euler equations, the dynamic model of the vehicle can be written as

$$
\begin{cases}
m\dot{\mathbf{v}}_B + S(\boldsymbol{\omega}_B)m\mathbf{v}_B = \mathbf{f}_{aero}(\mathbf{v}_B, \boldsymbol{\omega}_B, \mathbf{u}, \mathbf{w}) + m\,{}^{B}_{I}R\,[0\ 0\ g]^T \\
I\dot{\boldsymbol{\omega}}_B + S(\boldsymbol{\omega}_B)I\boldsymbol{\omega}_B = \mathbf{n}_{aero}(\mathbf{v}_B, \boldsymbol{\omega}_B, \mathbf{u}, \mathbf{w})
\end{cases},
\tag{4}
$$

where $m \in \mathbb{R}^+$ and $I \in \mathbb{R}^{3\times3}$ denote the aircraft's mass and moment of inertia, respectively; g denotes the gravitational acceleration; and $\mathbf{f}_{aero}, \mathbf{n}_{aero} : (\mathbb{R}^3, \mathbb{R}^3, \mathbb{R}^{n_u}, \mathbb{R}^{n_w}) \to \mathbb{R}^3$ represent the external forces and moments acting on the body, which are in general functions of the body velocities $\mathbf{v}_B$ and $\boldsymbol{\omega}_B$, control inputs $\mathbf{u} \in \mathbb{R}^5$, and wind disturbances $\mathbf{w} \in \mathbb{R}^3$. The control vector $\mathbf{u} = [T, \delta_e, \delta_{ac}, \delta_{ad}, \delta_r]^T$ comprises the propeller generated thrust δ_t and the surface deflections for the elevator δ_e, aileron common mode δ_{ac}, aileron differential mode δ_{ad}, and rudder δ_r.

The complete dynamic model of the aircraft can be written as

$$
\begin{cases}
\dot{\mathbf{v}}_B = \mathbf{f}\,(\mathbf{v}_B, \boldsymbol{\omega}_B, \mathbf{u}, \mathbf{w}) + \mathbf{f}_g\,(\phi_B, \theta_B) \\
\dot{\boldsymbol{\omega}}_B = \mathbf{n}\,(\mathbf{v}_B, \boldsymbol{\omega}_B, \mathbf{u}, \mathbf{w}) \\
{}^{I}\dot{\mathbf{p}}_B = {}^{I}_{B}R\,\mathbf{v}_B \\
\dot{\boldsymbol{\lambda}}_B = Q(\phi_B, \theta_B)\,\boldsymbol{\omega}_B
\end{cases},
\tag{5}
$$

where

$$
\mathbf{f} = m^{-1}\mathbf{f}_{aero} - S(\boldsymbol{\omega}_B)\mathbf{v}_B,
$$
$$
\mathbf{n} = I^{-1}\mathbf{n}_{aero} - I^{-1}S(\boldsymbol{\omega}_B)I\boldsymbol{\omega}_B,
$$
$$
\mathbf{f}_g = {}^{B}_{I}R[0\ 0\ g]^T = R_X(\phi_B)^T R_Y(\theta_B)^T[0\ 0\ g]^T
$$

A. SimAirDyn Dynamic Model

SimAirDyn is an aircraft dynamic model designed for effective control system design and flight envelope expansion. The aircraft's dynamics can be described using a six degree of freedom rigid body dynamic model (such as the one presented in (5)), which is driven by forces and moments that explicitly include the effects of the propeller, fuselage, wings, and gravity.[14–16] The remaining components, namely the landing

American Institute of Aeronautics and Astronautics

gear and the antennas, which have a smaller impact on the overall behavior of the aircraft dynamic model, are not included in the simulator and will naturally be treated as disturbances by the control system.

The aircraft nonlinear simulation model SimAirDyn was tuned to adequately capture the essential behavior of the actual vehicle for a large operational flight envelope.[15, 16] The most important model parameters are the dimensionless aerodynamic force and torque coefficients, which can be obtained from a Taylor series expansion of the force and torque functions about selected operating regimes.[16] Typically these values are experimentally obtained in a wind tunnel. Alternatively, software packages exist that allow one to obtain reasonably good approximations of wind-tunnel experiments. One of these software packages is LinAir 4 from Desktop Aeronautics. LinAir 4 is an aircraft geometry modeler that provides a wide range of aerodynamic analysis tools, based on computation of the aerodynamic characteristics of multi-element, nonplanar lifting surfaces.

The overall model resulting from the integration of the abovementioned components is a highly coupled nonlinear dynamic system. However, analysis of the mission objectives will help to establish the relevant flight regimes, such as forward flight, coordinated turn, take-off, and landing, whose independent modeling can yield simpler and more effective and intuitive dynamic systems. This paper focuses on the forward flight and coordinated turn regimes, whereas a companion paper addresses the approach and landing phases.[17]

The resulting dynamic descriptions for both the full nonlinear model and the simplified models are expressed in state-space form and were used to develop a realistic aircraft simulation model on a PC using MATLAB/Simulink. The simplified models for the different flight regimes were validated against the full nonlinear aircraft simulation model, providing the working ground for the control design phase.

1. Linearization of the Aircraft Model

In this section, we briefly describe the natural modes of the linearized SimAirDyn model. The analysis is conducted assuming that the coupling between longitudinal and lateral-directional dynamics can be neglected and therefore the aircraft model can be approximated by two independent lower order systems. The trimming condition considered corresponds to a level flight trajectory followed at the speed of 30 m/s.

2. Longitudinal Modes

In order to study the longitudinal dynamics of the aircraft, we consider the following state vector

$$\mathbf{x} = [u/V \quad \alpha \quad q \quad \theta_B]^T, \tag{6}$$

where $V = \|v_B\|$ is the body linear speed and $\alpha = \text{atan}(w/v)$ the angle of attack. Recall that, according to the notation adopted, the body velocities are denoted by $\mathbf{v}_B = [u \ v \ w]^T$ and $\boldsymbol{\omega}_B = [p \ q \ r]^T$, and the Euler angles by $\boldsymbol{\lambda}_B = [\phi_B \ \theta_B \ \psi_B]^T$.

The linearized longitudinal dynamics typically have two pairs of complex conjugate poles, corresponding to the short and long-period longitudinal modes. The short-period longitudinal mode excites primarily the angle of attack α, pitch angle θ_B and pitch angle derivative $q = \dot{\theta}_B$. The model aircraft under analysis revealed, for this mode, an undamped natural frequency $\omega_n = 24.41$ rad/s and a damping ratio $\xi = 0.85$.

The long-period longitudinal mode, also called phugoid, acts mainly on the normalized longitudinal velocity, u/V, and pitch angle, θ_B. Physically, it can be interpreted as an oscillation in altitude, with successive transfers between kinetic and potential energy. The undamped natural frequency and the damping ratio that characterize the long-period longitudinal mode of the present model are given by $\omega_n = 0.32$ rad/s and $\xi = 0.10$, respectively.

3. Lateral Directional Modes

For the study of the lateral-directional modes of the linear model, the following state vector is used

$$\mathbf{x} = [v/V \quad p \quad \phi_B \quad r]^T \tag{7}$$

The linearized lateral-directional dynamics of the aircraft have a pair of complex conjugate poles and two real poles, corresponding to three modes. These are the so-called roll subsidence, Dutch-roll, and spiral mode.

The roll subsidence mode is associated with the fastest real pole located at -205.1 rad/s. It influences mainly the roll angle ϕ_B and roll velocity p, having little or no effect on both the approximate sideslip angle

American Institute of Aeronautics and Astronautics

given by $\arcsin(v/V) \simeq v/V$ and the approximate yaw angle derivative given by r. This pole dictates the behavior of the airplane in a pure roll motion, where all states remain constant, except for the roll angle.

The slowest pole is associated with the spiral mode of the aircraft. For the current linear model, the pole is located at 0.023 rad/s. Due to this instability, the aircraft will tend to deviate from its straight line path and describe a spiral trajectory of decreasing radius. The spiral mode is characterized by a coupled roll/yaw motion.

Finally, the pair of complex conjugate poles is associated with the Dutch-roll mode. For the present aircraft and trimming conditions, this mode has an undamped natural frequency of $\omega_n = 11.81$ rad/s and a damping ratio $\xi = 0.14$. This mode exhibits a phase difference of about 180° between roll and yaw angles, which results in an oscillation of the aircraft's center of mass about a straight line with direction given by the average velocity of the airplane.

III. Path-dependent Error Dynamic Model

Bearing in mind that the goal of this work is to design a controller that steers the vehicle along a desired path, while satisfying a coordinate turn constraint, we describe in this section the transformation applied to the vehicle dynamic model (5), which results in an error dynamic model that can be used for control purposes. This error dynamic model follows closely the framework defined in Reference 8. In order to define this error space, we must first introduce two coordinate frames relating the vehicle and the desired path, Γ. These are the tangent frame $\{T\}$ and the desired body frame $\{C\}$, shown in Figure 2. Both coordinate frames move along the path attached to the point on the reference path closest to the vehicle. The difference between the two lies in the fact that $\{T\}$ is always aligned with the tangent to the path, whereas $\{C\}$ provides the desired body orientation.
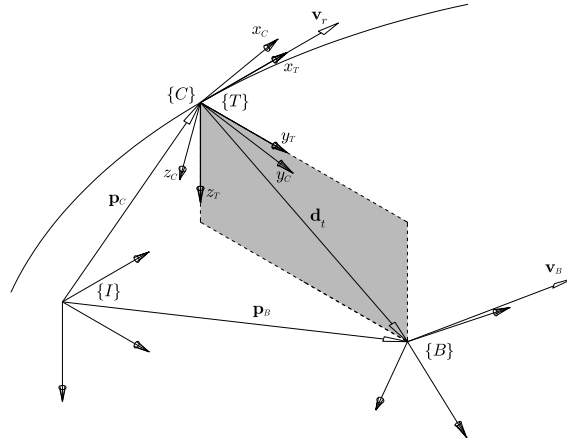

Figure 2. Coordinate frames: inertial $\{I\}$, body $\{B\}$, tangent $\{T\}$, and desired body frame $\{C\}$

A. The Tangent Frame $\{T\}$ and Desired Body Frame $\{C\}$

Let the desired path Γ be a smooth three-dimensional curve parameterized by the arc-length s. The tangent frame $\{T\}$ can be defined as a coordinate frame that moves along Γ and whose orientation relative to $\{I\}$ is given by

$$\,^I_T R(s) = [\mathbf{t}(s)\ \mathbf{n}(s)\ \mathbf{b}(s)] \in \mathrm{SO}(3), \tag{8}$$

where $\mathbf{t}(s)$ is the tangent, $\mathbf{n}(s)$ the signed normal, and $\mathbf{b}(s)$ the binormal to the path at the point specified by s. A formal definition of the tangent coordinate frame $\{T\}$ and a derivation of the equations ruling its motion along the curve can be found in Reference 8.

According to the definition of $\{T\}$, it is straightforward to show that $i)$ the linear velocity $\mathbf{v}_T = \,^T_I R\,^I \dot{\mathbf{p}}_T \in \mathbb{R}^3$ takes the form

$$\mathbf{v}_T = V_T [1\ 0\ 0]^T, \tag{9}$$

American Institute of Aeronautics and Astronautics

where $V_T = \dot{s} \in \mathbb{R}$ gives the speed with which the tangent frame is moving along the curve; *ii)* the motion of ${}^I_T R$ is ruled by the Serret-Frenet formulas, which can be written in compact form as

$$
{}^I_T\dot{R} = \frac{\mathrm{d}({}^I_T R)}{\mathrm{d}s}\,\dot{s} = V_T\,{}^I_T R\, S([\tau\ 0\ \kappa]^T);
\tag{10}
$$

and *iii)* the angular velocity $\boldsymbol{\omega}_T = {}^T_I R\,{}^I\boldsymbol{\omega}_T$ is therefore given by

$$
\boldsymbol{\omega}_T = V_T[\tau\ 0\ \kappa]^T.
\tag{11}
$$

The tangent frame $\{T\}$ is very similar to the commonly used Serret-Frenet frame. The main difference is that in some circumstances the y and z axes have opposite directions. The y axis of the Serret-Frenet frame (given by the normal to the path) always points toward the "inside" of the curve, implying that the frame is not continuous at inflection points. In the present case, the direction of the normal and binormal vectors is selected in order to preserve the continuity of $\{T\}$.

To account for the fact that the vehicle may take different orientations or even rotate with respect to the reference path, we consider the desired body frame $\{C\}$, whose orientation can be represented by the Z-Y-X Euler angles $\boldsymbol{\lambda}_C = [\phi_C\ \theta_C\ \psi_C]^T$, $\theta_C \in\ ]-\pi/2, \pi/2[$, $\phi_C, \psi_C \in \mathbb{R}$. Using the expressions for the tangent velocities $\mathbf{v}_T$ and $\boldsymbol{\omega}_T$ and assuming that $\{C\}$ does not rotate with respect to $\{T\}$, the linear and angular velocities of $\{C\}$ can be written as $\mathbf{v}_C = {}^C_T R\,\mathbf{v}_T$ and $\boldsymbol{\omega}_C = {}^C_T R\,\boldsymbol{\omega}_T$, respectively. Then, the derivative of $\boldsymbol{\lambda}_C$ can be written as

$$
\dot{\boldsymbol{\lambda}}_C = Q(\phi_C, \theta_C)\,{}^C_T R\,\boldsymbol{\omega}_T.
\tag{12}
$$

B. Error Space Definition

To define an error vector whose convergence to zero guarantees convergence to the path, the tangent frame is constrained to move along the path such that the distance vector $\mathbf{d} = {}^I\mathbf{p}_B - {}^I\mathbf{p}_T$ lives in the plane perpendicular to the tangent vector $\mathbf{t}$ (see Figure 2). It follows immediately that, when expressed in $\{T\}$, the distance vector has no x-component, i.e.

$$
{}^T_I R\,\mathbf{d} = [0\ \mathbf{d}_t^T]^T,\ \mathbf{d}_t = [d_y\ d_z]^T \in \mathbb{R}^2,
\tag{13}
$$

and simple manipulations show that the speed of the tangent frame is given by

$$
\dot{s} = V_T = \frac{1}{1 - \kappa\,d_y}\begin{bmatrix}1\ 0\ 0\end{bmatrix}{}^T_B R\,\mathbf{v}_B
\tag{14}
$$

and the motion of $\mathbf{d}_t$ is ruled by

$$
\dot{\mathbf{d}}_t = V_T\tau\begin{bmatrix}0 & 1\\ -1 & 0\end{bmatrix}\mathbf{d}_t + \begin{bmatrix}0 & 1 & 0\\ 0 & 0 & 1\end{bmatrix}{}^T_B R\,\mathbf{v}_B.
\tag{15}
$$

In addition to ensuring convergence in position, we are also interested in guaranteeing convergence in velocity and orientation. To this end, we introduce the reference speed V_r and define the linear and angular reference velocities for the tangent frame as $\mathbf{v}_r = V_r[1\ 0\ 0]^T$ and $\boldsymbol{\omega}_r = V_r[\tau\ 0\ \kappa]^T$, respectively, and we consider the following error vector definition

$$
\mathbf{x}_e = \begin{bmatrix}\mathbf{v}_e\\ \boldsymbol{\omega}_e\\ \mathbf{d}_t\\ \boldsymbol{\lambda}_e\end{bmatrix} = \begin{bmatrix}\mathbf{v}_B - {}^C_T R\,\mathbf{v}_r\\ \boldsymbol{\omega}_B - {}^C_T R\,\boldsymbol{\omega}_r\\ \Pi\,{}^T_I R\,({}^I\mathbf{p}_B - {}^I\mathbf{p}_T)\\ \boldsymbol{\lambda}_B - \boldsymbol{\lambda}_C\end{bmatrix} \in \mathbb{R}^{11},
\tag{16}
$$

where the matrix Π is given by

$$
\Pi = \begin{bmatrix}0 & 1 & 0\\ 0 & 0 & 1\end{bmatrix}.
$$

It is straightforward to verify that the vehicle follows a path Γ with speed $V_T = V_r$, relative angular velocity ${}^T\boldsymbol{\omega}_B = {}^T\boldsymbol{\omega}_C$, and orientation $\boldsymbol{\lambda}_B = \boldsymbol{\lambda}_C$ if and only if $\mathbf{x}_e = \mathbf{0}$. Moreover, it is easy to see that there is

American Institute of Aeronautics and Astronautics

a nonlinear transformation between the original state vector $\mathbf{x}_B = [\mathbf{v}_B^T \ \boldsymbol{\omega}_B^T \ ^I\mathbf{p}_B^T \ \boldsymbol{\lambda}_B^T]^T \in \mathbb{R}^{12}$ and the state vector given by $[\mathbf{x}_e^T \ s]^T$ and that, in general, the time derivative of $\mathbf{x}_e$ will take the form $\dot{\mathbf{x}}_e = \mathbf{f}_e(\mathbf{x}_e, s, \mathbf{u}, \mathbf{w})$. However, we will see shortly that the dependence on the arc-length s can be eliminated by restricting the references to satisfy a trimming condition.

It is well know that a vehicle with dynamics described by (5) is said to satisfy a trimming condition if $\dot{\mathbf{v}}_B = 0$, $\dot{\boldsymbol{\omega}}_B = 0$, and $\dot{\mathbf{u}} = 0$ with $\mathbf{w} = 0$, or equivalently, if the vehicle follows a straight line path or a z-aligned helix with constant speed and constant orientation relative to the path. Then, the reference is guaranteed to satisfy a trimming condition if $\dot{V}_r = 0$, $\dot{\kappa} = 0$, $\dot{\tau} = 0$, $^T\boldsymbol{\omega}_C = 0$, $\boldsymbol{\lambda}_T = [0 \ \gamma_T \ \psi_T]^T$, and $\dot{\psi}_T = \text{sign}(\kappa)V_T\sqrt{\kappa^2 + \tau^2}$. For helices, the flight path angle is given by $\gamma_T = \text{atan}(-\tau/\kappa)$, whereas for straight lines γ_T is a predefined constant. Under these constraints, the error dynamics can be written as

$$\begin{cases} \dot{\mathbf{v}}_e = \mathbf{f}(\mathbf{v}_B, \boldsymbol{\omega}_B, \mathbf{u}, \mathbf{w}) + \mathbf{f}_g(\phi_B, \theta_B) \\ \dot{\boldsymbol{\omega}}_e = \mathbf{n}(\mathbf{v}_B, \boldsymbol{\omega}_B, \mathbf{u}, \mathbf{w}) \\ \dot{\mathbf{d}}_t = V_T\tau \begin{bmatrix} 0 & 1 \\ -1 & 0 \end{bmatrix} \mathbf{d}_t + \begin{bmatrix} 0 & 1 & 0 \\ 0 & 0 & 1 \end{bmatrix} {}_B^T R \, \mathbf{v}_e \\ \dot{\boldsymbol{\lambda}}_e = Q(\phi_B, \theta_B)\boldsymbol{\omega}_B - \text{sign}(\kappa)V_T\sqrt{\kappa^2 + \tau^2} \, [0 \ 0 \ 1]^T \end{cases} \qquad (17)$$

A simple inspection of (17) reveals that no term depends explicitly on s. Even the rotation ${}_B^T R$, which apparently depends on $\psi_T(s)$ can be rewritten as ${}_B^T R = R_Y(\theta_T)^T R_Z(\psi_{ct} + \psi_e)R_Y(\theta_B)R_X(\phi_B)$, where ψ_{ct} denotes the constant difference $\psi_C - \psi_T$. Therefore, the error state equations can be written in compact form as

$$\dot{\mathbf{x}}_e = \mathbf{f}_e(\mathbf{x}_e, \boldsymbol{\eta}, \mathbf{u}), \qquad (18)$$

where the constant vector $\boldsymbol{\eta} = [V_r, \dot{\psi}_r, \gamma_T, \psi_{ct}, \phi_C, \theta_C]^T$ completely characterizes the reference trimming condition.

C. The Coordinate Turn Constraint

As referred earlier in the text, it is well-known that an aircraft can describe a z-aligned helix at constant speed and constant orientation relative to the path, while satisfying a trimming condition. In this work, we are also interested in enforcing a coordinated turn constraint.

Though in the case of small UAVs the question of ensuring the comfort of passengers is not present, implementing a coordinated turn constraint to describe a turning maneuver continues to be a relevant solution. It brings benefits in terms of efficiency and robustness due to the rudder's small size and does not require explicit dynamic inversion computations that are required to obtain, in real time, the steady state values for the actuators about other steady turn trimming conditions.

An aircraft is said to describe a coordinated turn maneuver if it verifies a trimming condition and the aerodynamical forces have no component along the y-axis of the body frame. Since at trimming the body velocities and control input satisfy $\dot{\mathbf{v}}_B = 0$, $\dot{\boldsymbol{\omega}}_B = 0$, and $\dot{\mathbf{u}} = 0$, we can rewrite the Newton equation given in (4) as

$$S(\boldsymbol{\omega}_B)m\mathbf{v}_B = \mathbf{f}_{aero}(\mathbf{v}_B, \boldsymbol{\omega}_B, \mathbf{u}, \mathbf{w}) + \mathbf{f}_g(\phi_B, \theta_B).$$

Then, the coordinated turn condition is verified if the aircraft's orientation is such that $[0 \ 1 \ 0]\mathbf{f}_{aero} = 0$ and consequently the y-components of the gravitational and centripetal forces coincide, that is,

$$[0 \ 1 \ 0]S(\boldsymbol{\omega}_B)m\mathbf{v}_B = [0 \ 1 \ 0]\mathbf{f}_g(\phi_B, \theta_B). \qquad (19)$$

Assuming that the trimming condition is specified by the linear speed V_r, curvature κ, torsion τ, roll angle ϕ_C, pitch angle θ_C, and yaw angle relative to the path ψ_{ct}, then the body velocities can be written as $\mathbf{v}_B = {}_T^C R\mathbf{v}_r$ and $\boldsymbol{\omega}_B = {}_T^C R\boldsymbol{\omega}_r$, where $\mathbf{v}_r = V_r[1 \ 0 \ 0]^T$, $\boldsymbol{\omega}_r = V_r[\tau \ 0 \ \kappa]^T$, and ${}_T^C R = R_X(\phi_C)^T R_Y(\theta_C)^T R_Z(\psi_{ct})^T R_Y(\gamma_T)$. Therefore (19) takes the form

$$\begin{aligned} \mathbf{e}_2^T {}_T^C R S(\boldsymbol{\omega}_r)\mathbf{v}_r &= \mathbf{e}_2^T R_X(\phi_C)^T R_Y(\theta_C)^T g\mathbf{e}_3 \\ \Leftrightarrow \mathbf{e}_2^T R_X(\phi_C)^T R_Y(\theta_C)^T (R_Z(\psi_{ct})^T V_r^2 \kappa \mathbf{e}_2 - g\mathbf{e}_3) &= 0 \end{aligned} \qquad (20)$$

where $\mathbf{e}_2 = [0 \ 1 \ 0]^T$ and $\mathbf{e}_3 = [0 \ 0 \ 1]^T$.

The methodology adopted in this paper to guarantee path-following convergence, involves not only the definition of the error space described above, but also the definition of an output tracking error $\mathbf{y}_e$ to be driven to zero at steady-state, by means of integral action. Defining an adequate $\mathbf{y}_e$ plays a key role in the current approach. This vector is required to have the same number of elements as the input vector and, to be of interest, it must be such that if $\dot{\mathbf{v}}_B = 0$, $\dot{\boldsymbol{\omega}}_B = 0$, $\dot{\mathbf{u}} = 0$, and $\mathbf{y}_e = 0$, then the characteristics of the trimming condition reached by the vehicle are completely determined. Namely, a coordinated turn can be enforced by including the respective constraint in $\mathbf{y}_e$. Moreover, for reasons of robustness, variables such as the roll, pitch, and yaw angles for which the uncertainty on the trimming values is high, should not be used as tracking variables.

In Section II, we considered an aircraft equipped with five actuation elements, which include the main thruster and a set of moving surfaces. In normal flight conditions, the thrust level command is usually applied in a stepwise manner to avoid fast wear out, unlike the surface deflections, which are typically commanded in a continuous manner. In the current approach, we assume that the thrust T is kept at a predefined constant value and, therefore, propose the following error vector

$$\mathbf{y}_e = \begin{bmatrix} y_{ct} \\ \Pi_{yz}\, {}^B_T R\, [0\ \mathbf{d}_t^T]^T \\ \delta_{a_c} \end{bmatrix}, \tag{21}$$

where the first component specifies the coordinate turn error given by

$$y_{ct} = \mathbf{e}_2^T R_X(\phi_B)^T R_Y(\theta_B)^T (R_Z(\psi_T - \psi_B)V_T^2 \kappa \mathbf{e}_2 - g\mathbf{e}_3). \tag{22}$$

This tracking error was chosen so as to guarantee that at steady-state

i) path-following convergence is achieved, since the y and z components of the distance vector expressed in the body frame converge to zero;

ii) the aircraft performs a coordinated turn, by enforcing the respective constraint;

iii) the aileron common mode δ_{a_c} is set to zero and thereby a washout on the common mode deflection is effectively implemented.

Notice that, in (21), neither the reference speed, V_r, nor the trimming values for the Euler angles ϕ_C, θ_C, and ψ_C are used as tracking variables. Based on the adopted control methodology, which will be described in the following sections, the constraints specified by the tracking error $\mathbf{y}_e$ allied to the fixed thrust restriction will automatically determine the values acquired by these variables at trimming.

Combining (18) and (21), the error space model of the aircraft can be written as

$$\mathcal{P}(\boldsymbol{\eta}) := \begin{cases} \dot{\mathbf{x}}_e = \mathbf{f}_e(\mathbf{x}_e, \boldsymbol{\eta}, \mathbf{u}, \mathbf{w}) \\ \mathbf{y}_e = \mathbf{g}(\mathbf{x}_e, \boldsymbol{\eta}) \end{cases}, \tag{23}$$

and since $\boldsymbol{\eta}$ is a constant parameter vector, the linearization of $\mathcal{P}(\boldsymbol{\eta})$ about the equilibrium point ($\mathbf{x}_e = 0$, $\mathbf{u} = \mathbf{u}_\eta$, $\mathbf{w} = 0$) results in a time-invariant system of the form

$$\mathcal{P}_l(\boldsymbol{\eta}) := \begin{cases} \delta\dot{\mathbf{x}}_e = A_e(\boldsymbol{\eta})\delta\mathbf{x}_e + B_e(\boldsymbol{\eta})\delta\mathbf{u} + B_{w_e}(\boldsymbol{\eta})\delta\mathbf{w} \\ \delta\mathbf{y}_e = C_e(\boldsymbol{\eta})\delta\mathbf{x}_e \end{cases}, \tag{24}$$

where $A_e(\boldsymbol{\eta})$, $B_e(\boldsymbol{\eta})$, $B_{w_e}(\boldsymbol{\eta})$, and $C_e(\boldsymbol{\eta})$ are the Jacobian matrices evaluated at the equilibrium point and parameterized by $\boldsymbol{\eta}$. Analytical expressions for these matrices can be found in Reference 8.

IV.   Controller Synthesis

In this section, an LMI approach is used to tackle the continuous-time state feedback H_2 synthesis problem for polytopic LPV systems. Consider the LPV system represented in Figure 3 with realization

$$G(\boldsymbol{\xi}) = \begin{cases} \dot{\mathbf{x}} = A(\boldsymbol{\xi})\mathbf{x} + B_w(\boldsymbol{\xi})\mathbf{w} + B(\boldsymbol{\xi})\mathbf{u} \\ \mathbf{z} = C(\boldsymbol{\xi})\mathbf{x} + D(\boldsymbol{\xi})\mathbf{w} + E(\boldsymbol{\xi})\mathbf{u} \end{cases}, \qquad \mathbf{u}(t) = K\mathbf{x}(t), \tag{25}$$
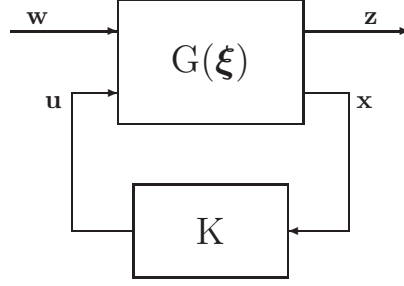
Figure 3. Feedback interconnection

where $\mathbf{x}$ is the state vector, $\mathbf{w}$ denotes the input vector of exogenous signals (including commands and disturbances), $\mathbf{z}$ is the output vector of errors to be reduced, and $\mathbf{u}$ is the vector of actuator signals. The connection between the generalized plant $G(\boldsymbol{\xi})$ and the error model described in Section III will be presented later in the text.

Without further assumptions, the synthesis problem for LPV systems involves testing an infinite number of LMIs. To overcome this problem, several different structures for the LPV system have been proposed which reduce the problem to that of solving a finite number of LMIs. In this work, we have adopted a polytopic description, which can be used to model a wide spectrum of systems and, as shown in the paper, is an adequate choice for the system at hand. In the following , $\mathrm{co}(\Xi_0)$ denotes the convex hull of Ξ_0 and $\mathrm{tr}(L)$ the trace of the matrix L.

Definition IV.1 (Polytopic LPV system)**.** The system (25) is said to be a polytopic LPV system with affine parameter dependence if the system matrix

$$S(\boldsymbol{\xi}) = \begin{bmatrix} A(\boldsymbol{\xi}) & B_w(\boldsymbol{\xi}) & B(\boldsymbol{\xi}) \\ C(\boldsymbol{\xi}) & D(\boldsymbol{\xi}) & E(\boldsymbol{\xi}) \end{bmatrix} \tag{26}$$

verifies $S(\boldsymbol{\xi}) = S^{(0)} + \sum_{j=1}^{n_p} S^{(j)} \xi_j$, for all $\boldsymbol{\xi} = [\xi_1 \ldots \xi_{n_p}]^T \in \Xi$, and the parameter set takes the form $\Xi = \mathrm{co}(\Xi_0)$, where

$$\Xi_0 = \{\boldsymbol{\xi} \in \mathbb{R}^{n_p} |\, \xi_i \in \{\underline{\xi}_i, \overline{\xi}_i\},\ \underline{\xi}_i \le \overline{\xi}_i,\ i = 1, \ldots, n_p\}\ .$$

We are interested in finding a solution to the continuous-time state feedback H_2 synthesis problem. Consider the static state feedback law given by $\mathbf{u} = K\mathbf{x}$ and let T_{zw} denote the closed-loop operator from $\mathbf{w}$ to $\mathbf{z}$. Then, the $\mathcal{H}_2$ synthesis problem can be described as that of finding a control matrix K that stabilizes the closed-loop system and minimizes the H_2 norm $\|T_{zw}\|_2$. Note that matrix $D(\boldsymbol{\xi})$ must satisfy $D(\boldsymbol{\xi}) = 0$ in order to guarantee that $\|T_{zw}\|_2$ is finite for every internally stabilizing and strictly proper controller. The technique used for controller design relies on results available in References 10 and 11, after being rewritten for the case of polytopic LPV systems.

Result IV.1. *A static state feedback controller guarantees the ζ upper-bound for the continuous-time H_2 norm of the closed-loop operator $T_{zw}(\boldsymbol{\xi})$ for all $\boldsymbol{\xi} \in \Xi$, that is,*

$$\|T_{zw}(\boldsymbol{\xi})\|_2 < \zeta, \forall \boldsymbol{\xi} \in \Xi \tag{27}$$

if there are real matrices $X = X^T > 0$, $Y > 0$, and W such that

$$\begin{bmatrix} A(\boldsymbol{\xi})\,X + X\,A(\boldsymbol{\xi})^T + B(\boldsymbol{\xi})\,W + W^T B(\boldsymbol{\xi})^T & B_w(\boldsymbol{\xi}) \\ B_w(\boldsymbol{\xi})^T & -I \end{bmatrix} < 0 \tag{28a}$$

$$\begin{bmatrix} Y & C(\boldsymbol{\xi})\,X + E(\boldsymbol{\xi})\,W \\ X\,C(\boldsymbol{\xi})^T + W^T E(\boldsymbol{\xi})^T & X \end{bmatrix} > 0 \tag{28b}$$

$$\mathrm{tr}\,(Y) < \zeta^2\ . \tag{28c}$$

for all $\boldsymbol{\xi} \in \Xi_0$. The respective controller gain matrix is given by $K = W\,X^{-1}$.

American Institute of Aeronautics and Astronautics

Additional closed-loop regional eigenvalues placement specifications for each plant $G(\boldsymbol{\xi})$ in the polytopic region identified with the parameter set Ξ can also be converted into design constraints resorting to the concept of LMI regions in the complex plane introduced in Reference 18. These constitute a generalization of the well known α stability region presented next.

Result IV.2. *The closed-loop system with realization* (25) *has all the eigenvalues in the semi-plane* $\lambda \in C$: $Re(\lambda) < -\alpha$ *for all* $\boldsymbol{\xi} \in \Xi$ *if matrices* $X = X^T > 0$ *and* W *exist such that the closed-loop Lyapunov inequality*

$$A(\boldsymbol{\xi})\,X + X\,A(\boldsymbol{\xi})^T + B(\boldsymbol{\xi})\,W + W^T\,B(\boldsymbol{\xi})^T + 2\alpha I < 0 \tag{29}$$

is satisfied for all $\boldsymbol{\xi} \in \Xi_0$.

This well known result can be generalized as follows. Let $L = [l_{ij}]$ and $M = [m_{ij}]$ be real symmetric matrices. An LMI region R_{lmi} is defined as an open domain in the complex plane that satisfies

$$\mathrm{R}_{lmi} = \{z \in \mathbf{C} : l_{ij} + m_{ij}z + m_{ji}\bar{z} < 0; \quad i,j = 1, ..., n\}. \tag{30}$$

This description can represent a large number of regions which are symmetric with respect to the real axis, such as conic sectors, half-planes, etc. Using the concept of LMI regions, Result IV.2 admits the following generalization, see Reference 18 for further details:

Result IV.3. *The closed-loop system with realization* (25) *has all the eigenvalues in the region* R_{cl} *defined by* (30) *for all* $\boldsymbol{\xi} \in \Xi$ *if a real symmetric matrix* $X > 0$ *exists such that the closed-loop generalized Lyapunov inequality*

$$l_{ij}X + m_{ij}(A(\boldsymbol{\xi})\,X + B(\boldsymbol{\xi})\,W) + m_{ji}(X\,A(\boldsymbol{\xi})^T + W^T\,B(\boldsymbol{\xi})^T) < 0; \quad i,j = 1, ..., n. \tag{31}$$

is satisfied.
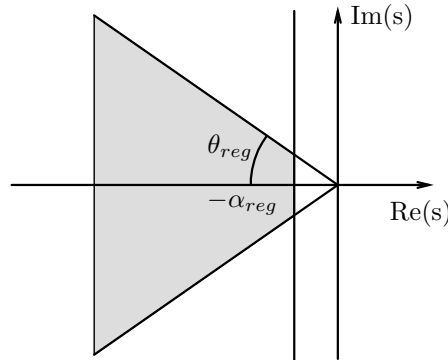
Figure 4. A typical closed-loop generalized stability region

In the present design case, the closed-loop eigenvalues are required to lie in the region depicted in Figure 4. Simple computations show that in this case (31) degenerates into

$$\begin{bmatrix} \sin(\theta_{reg})(\Upsilon(\boldsymbol{\xi}) + \Upsilon(\boldsymbol{\xi})^T) & \cos(\theta_{reg})(\Upsilon(\boldsymbol{\xi})^T - \Upsilon(\boldsymbol{\xi})) & 0 \\ \cos(\theta_{reg})(\Upsilon(\boldsymbol{\xi}) - \Upsilon(\boldsymbol{\xi})^T) & \sin(\theta_{reg})(\Upsilon(\boldsymbol{\xi}) + \Upsilon(\boldsymbol{\xi})^T) & 0 \\ 0 & 0 & \Upsilon(\boldsymbol{\xi}) + \Upsilon(\boldsymbol{\xi})^T + 2\alpha_{reg}X \end{bmatrix} < 0, \tag{32}$$

where $\Upsilon(\boldsymbol{\xi}, X, W) = A(\boldsymbol{\xi})\,X + B(\boldsymbol{\xi})\,W$ and parameters α_{reg} and θ_{reg} were set to $\alpha_{cl} = -0.1$, and $\theta_{cl} = 45^o$, respectively, so as to meet the desired closed-loop performance specifications. The optimal solution for the continuous-time H_2 control problem is approximated through the minimization of ζ subject to the LMIs presented in (28) and (32).

A.   Affine Parameter Dependent Approximation of the Error Dynamics

In this section, we describe the process of approximating the linearized error dynamics given in (18) by a polytopic LPV system with affine dependence on a given set of parameters. We consider the parameter vector $\boldsymbol{\xi} = [V_r \ \dot{\psi}_r \ \gamma_T]^T$ and partition the parameter domain into the 64 convex regions (each with 8 vertices), which result from the combination of intervals defined for each of the parameters. The values for these intervals, which are presented in Table 1, were selected to encompass a wide range of operating conditions. Notice the overlap between adjacent regions, which is used to implement an hysteresis commutation between controllers.

Table 1. Definition of the limits of the flight envelope regions

Parameters	Regions	
V_r	[19.5 24.25], [23.25 28], [27 31.75], [30.75 35.5]	(m/s)
$\dot{\psi}_r$	$[-0.41 \ -0.19]$, $[-0.21 \ 0.01]$, $[-0.01 \ 0.21]$, $[0.19 \ 0.41]$	(rad/s)
γ_T	$[-0.155 \ -0.07]$, $[-0.08 \ 0.005]$, $[-0.005 \ 0.08]$, $[0.07 \ 0.155]$	(rad)

Within each region, the state space matrices of the linearized error space dynamics were approximated by affine functions of $\boldsymbol{\xi}$ using Least Squares Fitting. The resulting system was evaluated at the vertices of each region, producing the finite set of state space matrices S_i, $i \in \{1, 2, \ldots, 8\}$ needed for control system design.

To access the validity of this approach, we compute a measure of the relative error between the original linearizations and the corresponding affine parameter dependent approximations. In the following, the dependence on $\boldsymbol{\xi}$ is omitted for reasons of simplicity. To establish a measure for the referred error, we consider the functions

$$\mathbf{y} = A_e \mathbf{x} + B_e \mathbf{u} + B_{w_e} \mathbf{w}, \quad \hat{\mathbf{y}} = \hat{A}_e \mathbf{x} + \hat{B}_e \mathbf{u} + \hat{B}_{w_e} \mathbf{w},$$

where A_e, B_e, and B_{w_e} are the original system matrices and $\hat{A}_e$, $\hat{B}_e$, and $\hat{B}_{w_e}$ the respective approximations. It is easy to see that the maximum absolute error produced, for example, by $A_e - \hat{A}_e$ can be computed element-wise as

$$g_{i_{\max}}(A_e, \hat{A}_e) = \max_{\mathbf{x}} \frac{|\mathbf{e}_i^T (A_e - \hat{A}_e) \mathbf{x}|}{\|\mathbf{x}\|} = \|\mathbf{e}_i^T (A_e - \hat{A}_e)\|,$$

where $\mathbf{e}_i$ is the vector with all elements equal to zero except for ith component, which is set to one. The corresponding relative gain error is given by

$$g_{i_{rel}}(A_e, \hat{A}_e) = \frac{g_{i_{\max}}(A_e, \hat{A}_e)}{\|\mathbf{e}_i^T A_e\|}. \tag{33}$$

Using (33) and similar expression involving the pairs $(B_e, \hat{B}_e)$ and $(B_{w_e}, \hat{B}_{w_e})$, the relative error measures were computed for a dense grid of operating points inside each region. The computations showed that the maximum value of each component $g_{i_{rel}}$ never exceeds 12%, whereas the mean maximum error over all regions is 5%. These results support the selection of the affine parameter dependent representation as adequate approximation of the aircraft model. To illustrate the results obtained, plots of the relative gain error $g_{1_{rel}}(A_e(\boldsymbol{\xi}), \hat{A}_e(\boldsymbol{\xi}))$, defined as a function of two of the parameters in $\boldsymbol{\xi} = [V_r \ \dot{\psi}_r \ \gamma_T]^T$ with the remaining one fixed, are presented in Figure 5.

B.   Synthesis Model and Controller Design

The linear state feedback controllers were required to meet the following design specifications:

Zero Steady State Error. Achieve zero steady state values for the error variable $\mathbf{y}_e$.

Bandwidth Requirements. The control loop bandwidth for the actuators channels should not exceed 10 rad/s ; this limit was selected to ensure that the actuators would not be driven beyond their normal actuation bandwidth.
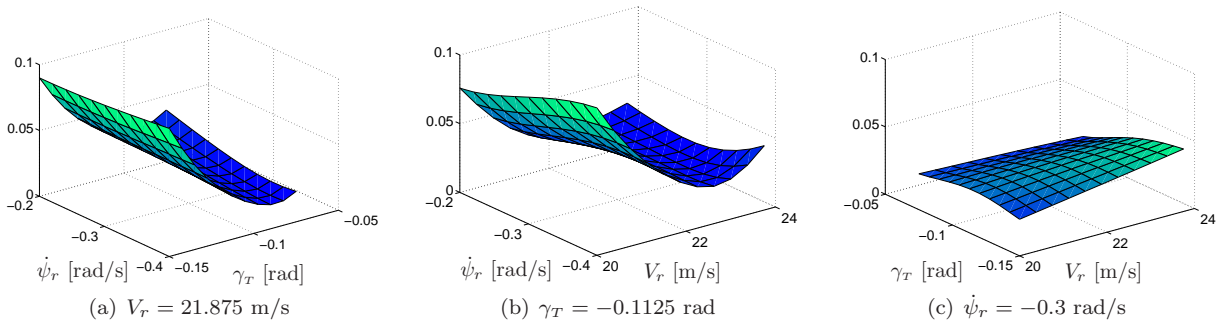
American Institute of Aeronautics and Astronautics

(a) $V_r = 21.875$ m/s (b) $\gamma_T = -0.1125$ rad (c) $\dot{\psi}_r = -0.3$ rad/s

Figure 5. Variation of the relative error measure $g_{1_{rel}}(A_e(\boldsymbol{\xi}), \hat{A}_e(\boldsymbol{\xi}))$ inside the first operating region.

Closed Loop Damping and Stability Margins. The closed loop eigenvalues should have a damping ratio of at least 0.7 and a real part of at least 0.1 rad/s. It was also required zero steady state deflection of the ailerons.

The first step in the controller design procedure is the development of a synthesis model that can serve as an interface between the designer and the H_2 controller synthesis algorithm. Consider the feedback system shown in Figure 6, where P is the discrete-time linear model of the aircraft error dynamics, and K is a state feedback controller to be designed. The augmented system G shown within the dashed line is the synthesis model, which is derived from the linear model of the plant by appending the depicted weights. In practice, the weights serve as tuning "knobs" which the designer can adjust to meet the desired performance specifications.
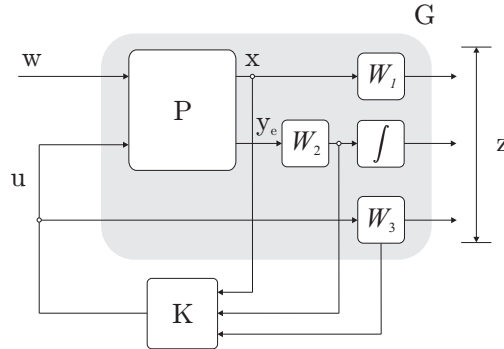
Figure 6. Synthesis model

The weight W_1 was set to $W_1 = \text{diag}([10^{-4}[1\ 10\ 1], [0.1\ 1\ 1], 10^{-4}[1\ 1\ 1\ 1\ 1]])$. To penalize the output tracking error, the weighting function W_2 was chosen as $W_2 = \text{diag}([10\ 1\ 1\ 10^{-3}])$. The weight W_3 on the actuation vector **u** was set to $W_3 = W_{3a}(s)I_4$, where the transfer function $W_{3a}(s)$ is given by

$$W_{3a}(s) = 10\frac{s+1}{s+10}.$$

The inclusion of these high-pass weights expedites the process of fine tuning the closed-loop bandwidths of the control inputs because it penalizes high frequency components of the actuation signals.

The final gain-scheduled implementation scheme, presented in Figure 7, was obtained using the D-methodology described in Reference 12. This methodology moves all integrators to the plant input, and adds differentiators where they are needed to preserve the transfer functions and the stability characteristics of the closed-loop system. The D-methodology implementation has several important features, which include the following: *i)* auto-trimming property - the controller automatically generates adequate trimming values for the actuation signals and for the state variables that are not required to track reference inputs; and *ii)* the implementation of anti-windup schemes is straightforward, due to the placement of the integrators at the plant input.

American Institute of Aeronautics and Astronautics
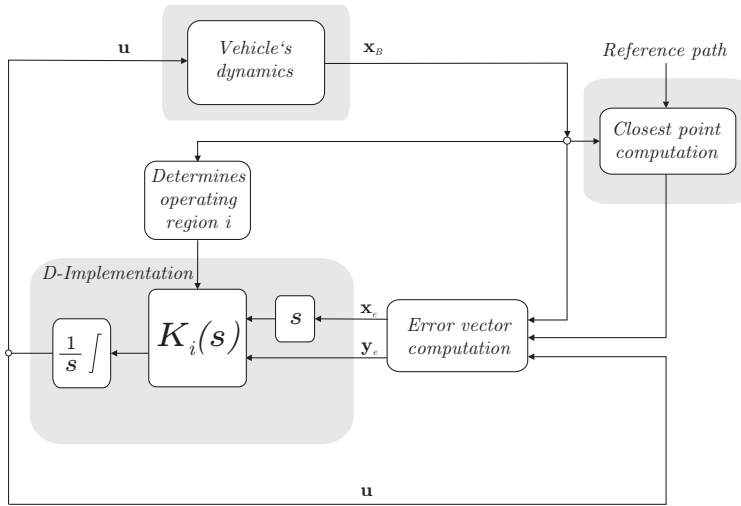
Figure 7. Implementation setup using gain scheduling and the D-methodology.

V.   Simulation Results

The simulation results presented in this section were obtained using the full nonlinear dynamic model of the aircraft described in Section II.A, which was implemented in MATLAB/Simulink. The simulations were conducted using atmospheric turbulence as a disturbance. This turbulence reflects random changes in wind direction and velocity. The wind velocity, at a given time t and position $\mathbf{r}$ is expressed as

$$\mathbf{w}(\mathbf{r}, t) = \mathbf{w_0}(\mathbf{r}, t) + \Delta\mathbf{w}(\mathbf{r}, t) \tag{34}$$

where $\mathbf{w}_0$ denotes the mean wind velocity and $\Delta\mathbf{w}$ represents the atmospheric turbulence, which is modeled as a random variable with a Dryden power spectrum.[16]

In the following, we present simulation results that illustrate the performance that can be achieved with the proposed control methodology. These simulations were obtained using a gain-scheduled controller with dynamic weights on the actuation, based on the the family of linear controllers synthesized for the regions defined in Section IV.A. The aircraft reference path considered is divided into three segments: *i)* a straight line path at constant altitude, *ii)* a circular path, and *iii)* a climbing helix. The parameters for each segment are presented in Table 2.

Figure 8 shows a 3D view of the path described by the aircraft in the absence of wind disturbances. Notice that during the second and third stages, the aircraft is banked to comply with the coordinated turn constraint defined in (20).

Table 2.   Reference path parameters

Thrust (N)	Radius (m)	γ_T (rad)
16	∞	0
17	200	0
37	200	0.1

Simulations results were obtained using two different intensities for the atmospheric disturbances. Because of the stochastic nature of the wind disturbances, and in order to obtain more accurate results, several simulations of the airplane were ran using different initialization seeds for the random number generators. The results presented correspond to the average over 5 of these parallel simulations. The time evolution was normalized with respect to speed so as to guarantee that the transitions between stages occur simultaneously.

In the first set of simulations, whose results are presented in Figures 9 and 10, a wind disturbance with mean speed of 0.5 m/s was used. For the second case, illustrated in Figures 11 and 12, a wind disturbance

American Institute of Aeronautics and Astronautics
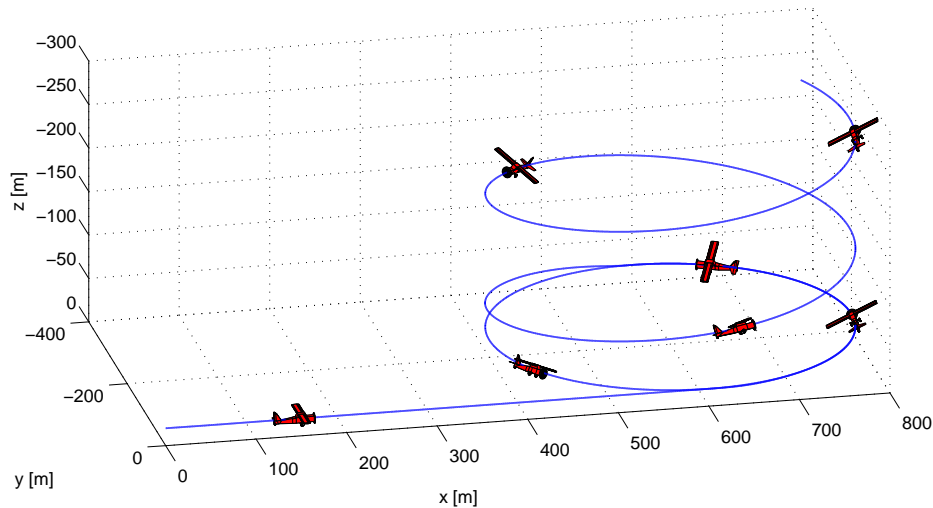
Figure 8. Path-following simulation result obtained in the absence of wind disturbances.

with mean speed of 3 m/s was considered. Figures 9 and 11 refer to the transition between the straight line and circular paths, whereas Figures 10 and 12 depict the second reference path transition. Notice that, due to the aircraft's large wingspan (3 m) and light weight (20 kg), even small wind disturbances can affect significantly its trajectory.

In Tables 3 and 4 we present the root mean square (RMS) values for the three wind velocities and the output tracking errors, which according to (21) comprise the distances d_y and d_z, the ailerons common mode δ_{a_c} and the coordinated turn error y_{ct} defined in (22). As shown in Figures 9-12, these tracking errors converge to zero at steady-state, thereby justifying the RMS analysis.

Table 3. RMS values for the wind velocities and output tracking errors - Circular path

Intensity	u_{wind} (m/s)	v_{wind} (m/s)	w_{wind} (m/s)	d_y (m)	d_z (m)	δ_{a_c} (rad)	y_{ct} (N)
Low	0.038153	0.031979	0.020199	0.0021737	0.0035252	1.7962e-005	0.049427
High	0.30628	0.25836	0.15206	0.035176	0.050906	0.00019511	0.37093

Table 4. RMS values for the wind velocities and output tracking errors - Helix path

Intensity	u_{wind} (m/s)	v_{wind} (m/s)	w_{wind} (m/s)	d_y (m)	d_z (m)	δ_{a_c} (rad)	y_{ct} (N)
Low	0.032861	0.034467	0.022728	0.0026061	0.005333	6.6319e-005	0.52537
High	0.24866	0.18649	0.14679	0.015521	0.024409	0.00013014	0.64799

The bandwidth limitation enforced by the dynamic weights is clearly visible in the signal activity exhibited by the actuators (see the subfigures (c) in Figures 9 through 12). The rate of the actuation stays within the predefined bandwidth (approximately 10 rad/s) and the valid operating limits of ±0.4 rad for the surface deflection angles are not exceeded, even during transitions between reference paths.

VI.   Conclusions

This paper presented a path-following controller for coordinated turn aircraft maneuvers. A nonlinear dynamic model of a small scale aircraft was constructed and used as the basis for the controller design and simulation. The design technique applied is based on an error space that fully describes the aircraft dynamic behavior in a given flight envelope and explicitly defines a tracking error, whose convergence to zero at steady-state guarantees both path-following and coordinated turn compliance. A polytopic LPV approximation of the error model was adopted to accurately represent the aircraft dynamics, within a
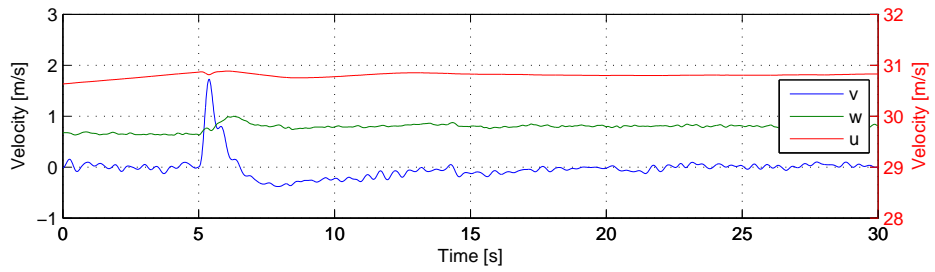
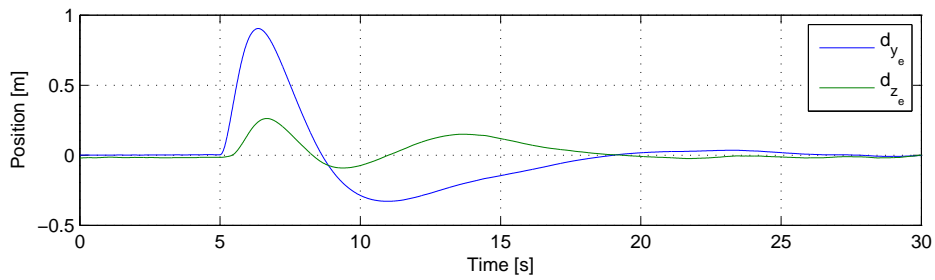American Institute of Aeronautics and Astronautics
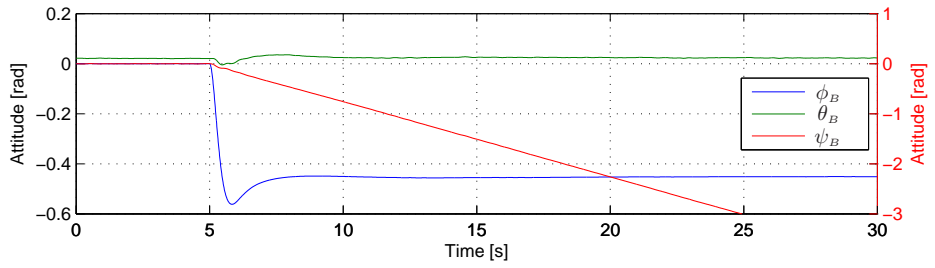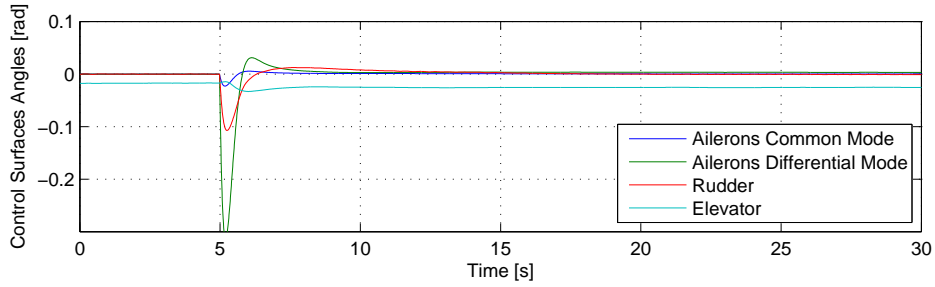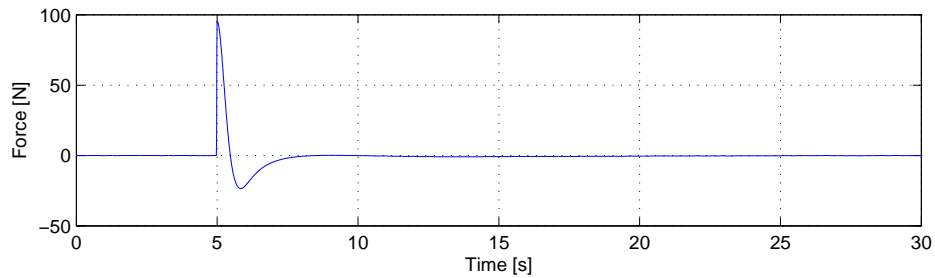
(a) Vehicle Body Velocity

(b) Vehicle Orientation
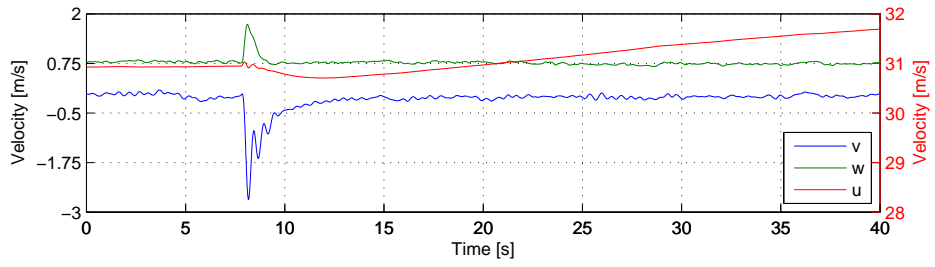

(c) Vehicle Actuation

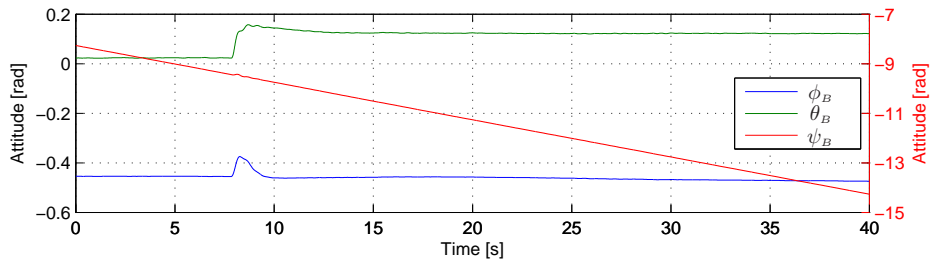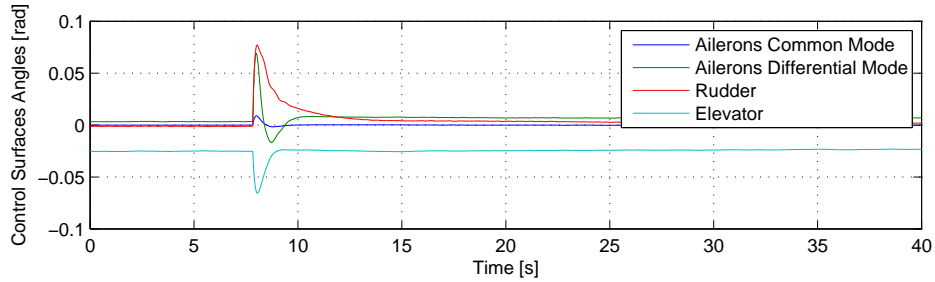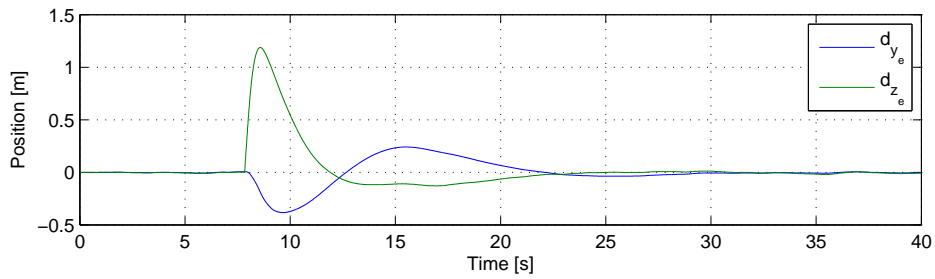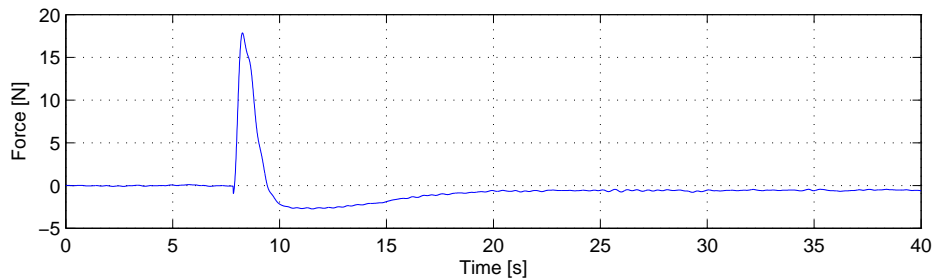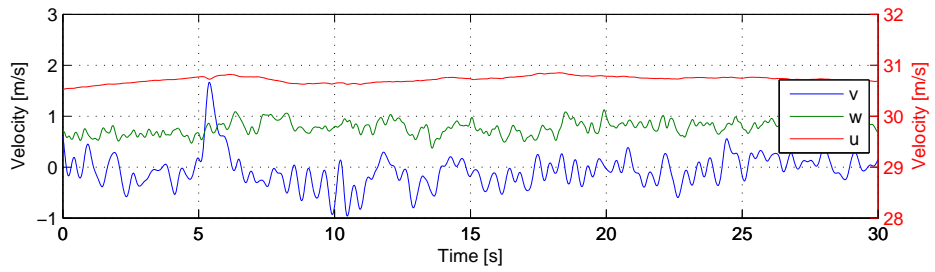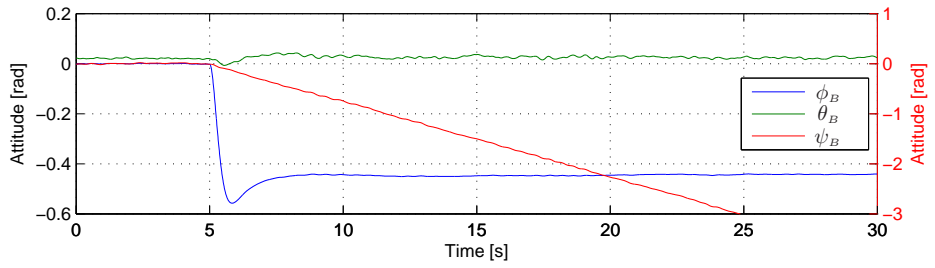(d) Vehicle Path-Following Error

(e) Vehicle Coordinated Turn Error

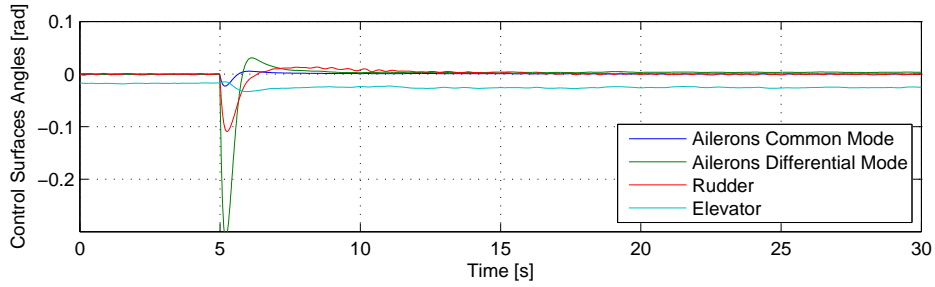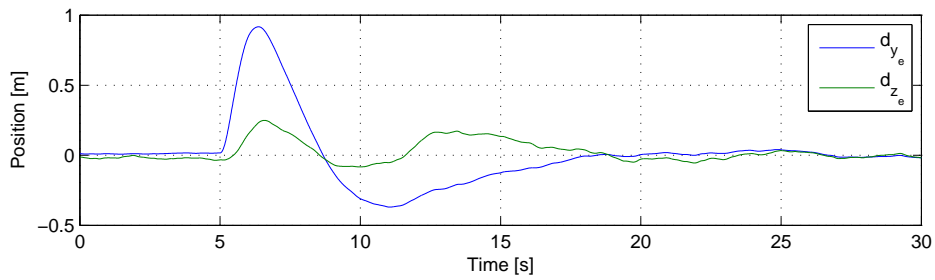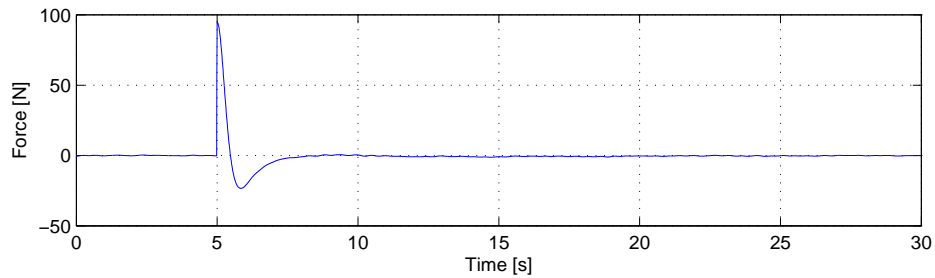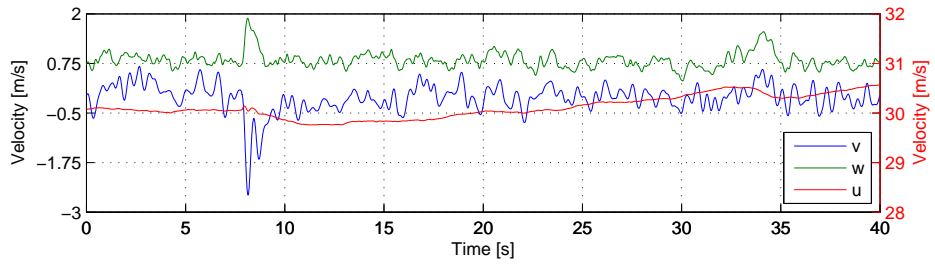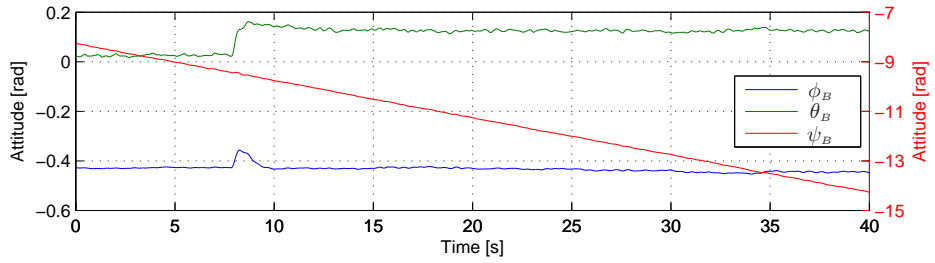**Figure 9. Aircraft simulation with low wind disturbances - Transition between straight line and circular trajectories**

American Institute of Aeronautics and Astronautics

(a) Vehicle Body Velocity

(b) Vehicle Orientation

(c) Vehicle Actuation

(d) Vehicle Path-Following Error

(e) Vehicle Coordinated Turn Error

Figure 10. Aircraft simulation with low wind disturbances - Transition between circular and helix trajectories

American Institute of Aeronautics and Astronautics

(a) Vehicle Body Velocity

(b) Vehicle Orientation

(c) Vehicle Actuation

(d) Vehicle Path-Following Error

(e) Vehicle Coordinated Turn Error

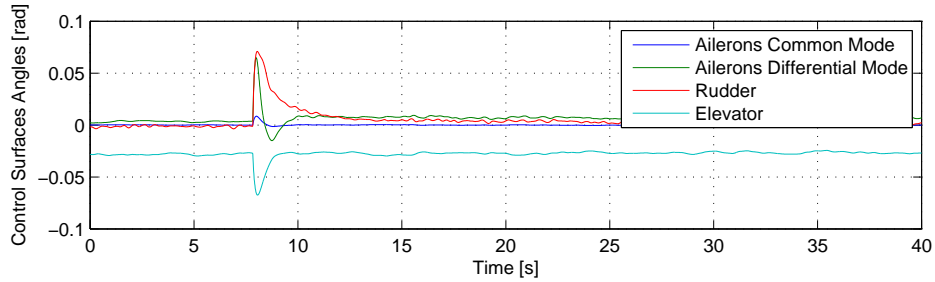**Figure 11. Aircraft simulation with high wind disturbances - Transition between straight line and circular trajectories**

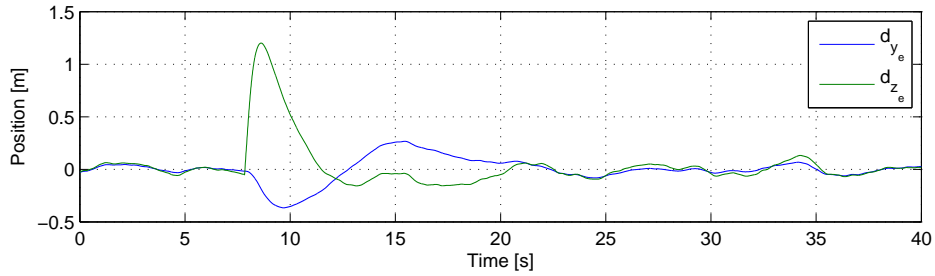American Institute of Aeronautics and Astronautics
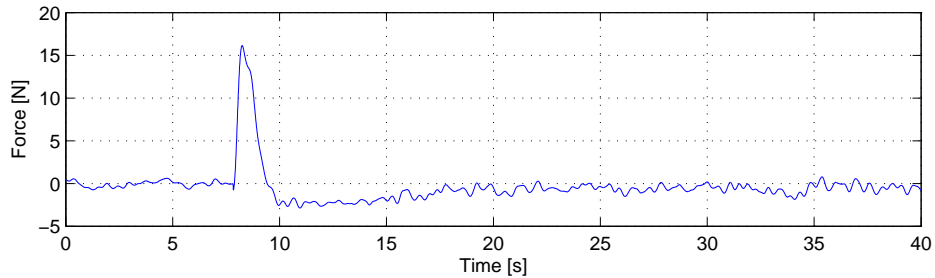
(a) Vehicle Body Velocity

(b) Vehicle Orientation

(c) Vehicle Actuation

(d) Vehicle Path-Following Error

(e) Vehicle Coordinated Turn Error

Figure 12. Aircraft simulation with high wind disturbances - Transition between circular and helix trajectories

American Institute of Aeronautics and Astronautics

predefined set of operating regions. An LMI-based H_2 controller design methodology for polytopic LPV systems was applied, which includes pole placement constraints and exploits dynamic weights to limit the actuation bandwidth. The full nonlinear controller was implemented using gain-scheduling control theory and tested in simulation with the nonlinear model of a small scale airplane. The simulation results obtained attest to the adequacy of the proposed path-following control methodology.

Acknowledgments

References

[1] Azam, S. N. and Singh, M., "Invertibility and Trajectory Control for Nonlinear Maneuvers of Aircraft," *AIAA Journal of Guidance, Control, and Dynamics*, Vol. 17, No. 1, 1994, pp. 192–200.

[2] Al-Hiddabi, N. H. and McClamrooh, S. A., "Trajectory tracking control and maneuver regulation control for the CTOL aircraft model," *Decision and Control, 1999. Proceedings of the 38th IEEE Conference on*, Vol. 2, 1999, pp. 1958–1963.

[3] Shue, S.-P., Sawan, M. E., and Rokhsaz, K., "Mixed H_2/H_∞ Method Suitable for Gain Scheduled Aircraft Control," *Journal of Guidance, Control, and Dynamics 1997*, Vol. 20, No. 4, 1999, pp. 699–706.

[4] Thompson, P. and Chiang, R., "H^∞ robust control synthesis for a fighter performing a coordinated bank turn," *Decision and Control, 1990., Proceedings of the 29th IEEE Conference on*, Praha, Czech Republic, 1990.

[5] Stevens, B. L. and Lewis, F. L., *Aircraft Control and Simulation, 2nd Edition*, Wiley-Interscience, 2003.

[6] Kaminer, I., Pascoal, A., Hallberg, E., and Silvestre, C., "Trajectory Tracking for Autonomous Vehicles: An Integrated Approach to Guidance and Control," *AIAA Journal of Guidance, Control, and Dynamics*, Vol. 21, No. 1, 1998, pp. 29–38.

[7] Silvestre, C., Pascoal, A., and Kaminer, I., "On the Design of Gain-Scheduled Trajectory Tracking Controllers," *International Journal of Robust and Nonlinear Control*, Vol. 12, 2002, pp. 797–839.

[8] Cunha, R., Antunes, D., Gomes, P., and Silvestre, C., "A Path-Following Preview Controller for Autonomous Air Vehicles," *AIAA Guidance Navigation and Control Conference, Keystone, CO, USA*, 2006.

[9] Boyd, S., Ghaoui, L. E., Feron, E., and Balakrishnan, V., *Linear Matrix Inequalities in Systems and Control Theory*, Society for Industrial and Applied Mathematics, SIAM, Philadelphia, PA, 1994.

[10] Ghaoui, L. E. and Niculescu, S. I., editors, *Advances in Linear Matrix Inequality Methods in Control*, Society for Industrial and Applied Mathematics, SIAM, Philadelphia, PA, 1999.

[11] Scherer, C. and Weiland, S., *Lecture Notes on Linear Matrix Inequalities in Control*, Dutch Institute of Systems and Control, 2000.

[12] Kaminer, I., Pascoal, A., Khargonekar, P., and Coleman, E., "A Velocity Algorithm for the Implementation of Gain-Scheduled Controllers," *Automatica*, Vol. 31, No. 8, 1995, pp. 1185–1191.

[13] Craig, J. J., *Introduction to Robotics and Control: Mechanics and Control, 2nd ed.*, Addison-Wesley Publishing Company, Massachusetts, 1989.

[14] Brederode, V., *Fundamentos de Aerodinmica Incompressvel*, Author's publication, 1997.

[15] Schmidt, L. V., *Introduction to Aircraft Flight Dynamics*, AIAA Education Series, 1998.

[16] Stengel, R. F., *Flight Dynamics*, Princeton University Press, Flight Dynamics.

[17] Rosa, P., Silvestre, C., Cabecinhas, D., and Cunha, R., "Autolanding Controller for a Fixed Wing Unmanned Air Vehicle," *AIAA Guidance and Control Conference (Submitted)*, 2007.

[18] Chilali, M. and Gahinet, P., "H_∞ design with pole placement constraints: an LMI approach," *IEEE Transactions on Automatic Control*, Vol. 41, No. 3, March 1996, pp. 358–367.

American Institute of Aeronautics and Astronautics